Electronic Supplementary Material (ESI) for Nanoscale.

Electronic Supplemental Information: Tuning interfacial two-component superconductivity in $CoSi_2/TiSi_2$ heterojunctions via $TiSi_2$ diffusivity

Shao-Pin Chiu, Vivek Mishra, Yu Li, Fu-Chun Zhang, Stefan Kirchner, and Juhn-Jong Lin

(Dated: April 18, 2023)

The anomalous proximity effect and its relation to the zero-bias conductance peak

Our study is based on T-shaped three-terminal devices. It was predicted by Asano and coworkers [1] that these T-shaped proximity devices detect triplet pairing in the superconductor through a novel mechanism referred to as the anomalous proximity effect (APE). This proximity effect relies on the formation of odd-frequency pairs in the normal metal part which in turn leads to a ZBCP. In order to further substantiate our conclusions, this section provides normalized zero-bias conductance spectra of our junctions measured in the S/N junction geometry which clearly demonstrates that the ZBCP observed in the T-shaped devices is due to the proximity of superconducting $CoSi_2/Si$, see Fig. S1.

Yet further evidence against an 'extrinsic' origin of the ZBCP comes from the conductance spectra obtained for different VE pairs as shown in Fig. 2(a) of the main part, which demonstrates that if the S/N interface remains outside of the VE pairs, no ZBCP is observed.

Finally, if the ZBCP in the T-shaped proximity structures were of extrinsic origin, an alternative mechanism causing the ZBCP should exist. The natural candidate would be occurrence of dynamic scattering at localized impurities, *i.e.*, the Kondo effect. The magnetic field and temperature dependence of the transport data are, however, incompatible with Kondo scattering. This is further corroborated by the fact that no magnetic impurities were detected in our devices.

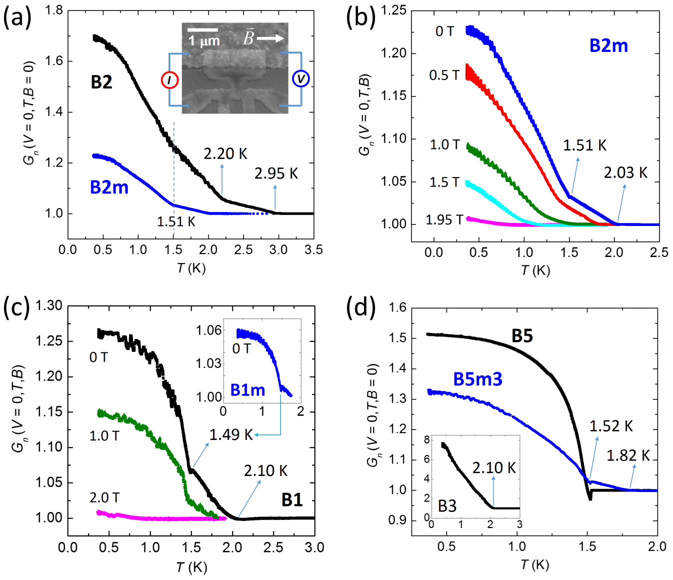

FIG. S1. Normalized zero-bias conductance $G_n(V = 0, T, B)$ for $CoSi_2/TiSi_2$ heterostructures measured in the S/N junction geometry, *i.e.*, using the 4-probe configuration schematically indicated in the inset of (a). (a) $G_n(0, T, 0)$ of devices B2 and B2m. The values of T_c^{onset} in B2 (2.95 and 2.20 K) and for $CoSi_2$ on Si(100) without a $TiSi_2$ interface, $T_c(CoSi_2/Si) = 1.51$ K, are indicated through arrows. Inset: SEM image of B2. (b) $G_n(0, T, B)$ of device B2m in several B fields. The value of T_c^{onset} at 2.03 K in this device is indicated. A small increase of G_n for $T < 0.85$ K at $B = 1.95$ T still occurs. (c) $G_n(0, T, B)$ of device B1 for various values of B. The inset shows $G_n(0, T, 0)$ of device B1m, with T_c^{onset} occurring at $T \gtrsim 1.8$ K. (d) $G_n(0, T, 0)$ of devices B5, B5m3, and B3 (inset). $T_c^{\text{onset}} = 1.82$ K, in B5m3 as indicated. Inset: T_c^{onset} at 2.10 K in B3 is indicated.

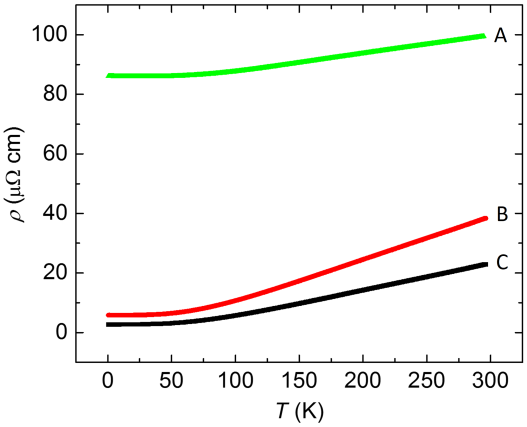

FIG. S2. Resistivity of $TiSi_2$/Si(100) films between 0.36 K and room temperature. All films have a thickness of 125 nm but were grown under different thermal annealing conditions which strongly affects the composition and thus the residual resistivity of the films. These conditions were 750°C for 1 h, 750°C for 1.5 h, and 800°C for 1 h for films A, B and C, respectively. Thus, film A is predominantly comprised of C49 $TiSi_2$, C is predominantly made up of C54, while film B's composition is some mixture of C49 and C54.

Device Fabrication and Characterization

Titanium films were deposited on an electron-beam lithographically patterned Si(100) substrate, and subsequently thermally annealed at a *thermal annealing temperature* (T_a) to form the normal-metal $TiSi_2$ component in the T-shaped proximity structure.

A decrease in the inverse residual resistivity, $1/\rho_N$, of the $TiSi_2$ N component of the T-shaped junctions is correlated with an increase in T_c^{onset} as evidenced in Fig. 4 of the main part. The diffusive properties of the $TiSi_2$ N component are primarily determined by the growth conditions of the devices and in particular by the annealing temperature. That T_a can have such an influence on the device properties is linked to the polymorphism of $TiSi_2$. The two phases of $TiSi_2$ relevant to our study are commonly known as the C49 phase and the C54 phase. While C49 phase is absent in the Ti-Si bulk equilibrium phase diagram, it is stabilized in microscale systems which appears to be linked to the availability or lack of nucleation sites for C54, see Ref. [2]. As a result, in thin layers of $TiSi_2$ on Si substrates the C49 phase appears to be stable up to a temperature that depends on the layer thickness [3].

A film comprised of predominantly the C49 (C54) $TiSi_2$ phase was obtained by annealing at 750°C (800°C) for about 1 hour [4]. A mixed C49-C54 $TiSi_2$ phase was obtained by applying an intermediate temperature (e.g., 780°C) for 1 hour.

Figure S2 shows the resistivity as a function of temperature for three pure $TiSi_2$/Si(100) films (without the $CoSi_2$ part) whose different thermal annealing conditions determine distinct phase compositions of $TiSi_2$/Si(100).

The C49 structure possesses a slightly larger unit cell volume than the C54 structure so that phase changes from C49 to C54 and vice versa are accompanied by strain [5]. Cross-sectional transmission electron microscopy studies furthermore reveal that the C49 phase has a smaller grain size ($\sim$ 50–300 nm), compared with that ($\sim$ 300–1000 nm) of the C54 phase. The carrier concentration in the C49 phase ($\approx 1.5 \times 10^{22}$ cm^{-3}) is more than one order of magnitude lower than that ($\approx 3 \times 10^{23}$ cm^{-3}) in the C54 phase [6]. Devices that formed at a comparatively high T_a are mainly composed of C54 and thus possess a correspondingly large diffusion constant which in turn is correlated with a T_c^{onset} that is roughly equal to T_c^{bulk}. This is the case of device B5 (as well as of those devices studied in Ref. [4]). Devices B1 and B2 (and B4) formed at a low T_a and consist predominantly of the C49 form of $TiSi_2$. At first sight, the results for device B3 that was formed at an intermediate T_a may seem confusing but can be rationalized by recalling that the formation of C54 requires particular nucleation sites which may be rare near the $CoSi_2$ interface. This may suggest that C49 grains are most stable near the $CoSi_2$ interface which in turn would suggest that the observed interface superconductivity is linked to the properties of the C49 phase.

Additional conductance spectra for $CoSi_2/TiSi_2$ T-shaped superconducting proximity structures

This section provides additional conductance spectra for the $CoSi_2/TiSi_2$ T-shaped superconducting proximity structures B1m (Fig. S3), B2m and B2 (Fig. S4), B3 (Fig. S5) and B5m3 as well as B5 (Fig. S6).

As in the main text, $G_n(V,T,B)$ denotes the normalized conductance, *i.e.*, it is normalized in terms of the low-temperature limit of the zero-bias conductance of the normal state. Further information is provided in the figure captions. $G_n(0,T,0)$ in device B2 shows a non-monotonic T dependence, increasing below 2.33 K and reaching a maximum at ~ 0.75 K, then followed by a small decrease to $\sim 110\%$ at 0.37 K. The $G_n(0,T,0)$ in device B3 shows a monotonic increase below 2.14 K, reaching $\sim 106\%$ at 0.37 K. This is shown in Figure 3(a) of the main text. $G_n(0,T,0)$ of device B5 is relatively small compared to that of device B5m3.

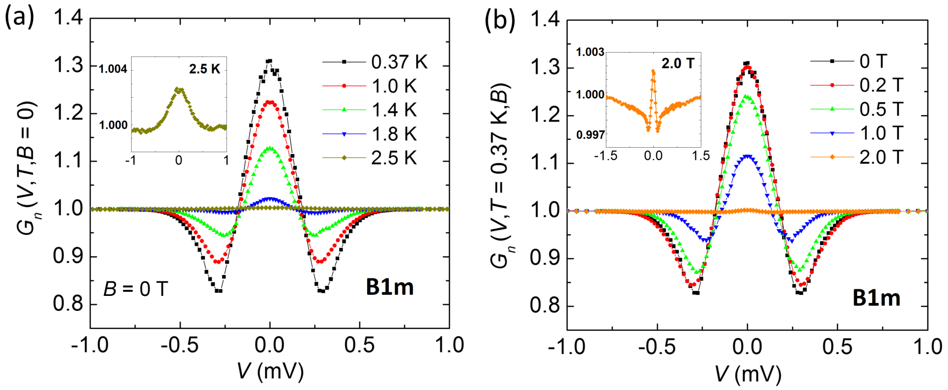

FIG. S3. Normalized conductance spectra of device B1m. (a) $G_n(V,T,0)$ measured at several T values. The amplitude of ZBCP gradually decreases with increasing T. The inset indicates that the ZBCP persists up to $T > 2.5$ K. (b) $G_n(V, 0.37\,\mathrm{K}, B)$ measured at several B values. The amplitude of ZBCP gradually decreases with increasing B. The inset indicates that the ZBCP persists up to $B > 2.0$ T.

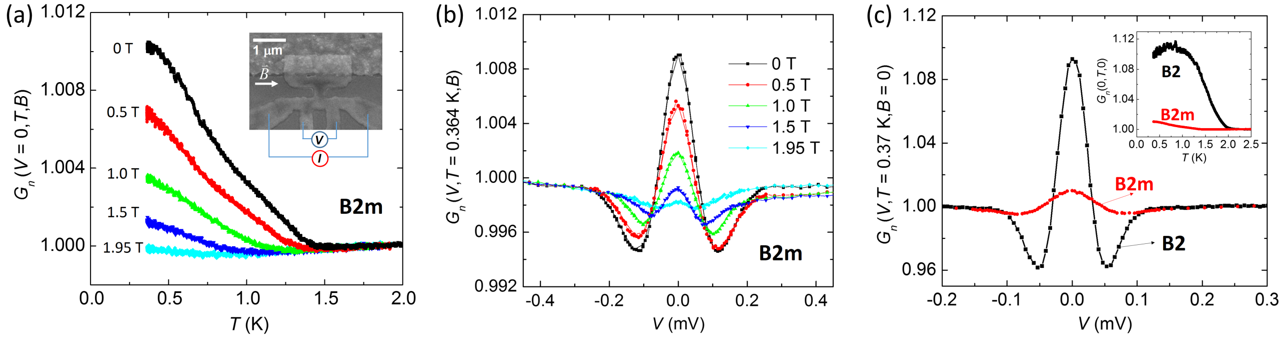

FIG. S4. Normalized conductance spectra of device B2m. (a) $G_n(0,T,B)$ for several B values. With increasing B, $G_n(0,T,B)$ is gradually suppressed. The inset shows an SEM image of the device and the schematic 4-probe configuration. (b) Finite-bias $G_n(V, 0.364\,\mathrm{K}, B)$ for the same values of B as in (a). A close inspection indicates that the ZBCP persists up to at least 1.95 T. (c) Comparison of $G_n(V, 0.37\,\mathrm{K}, 0)$ of devices B2 and B2m. Inset: $G_n(0,T,0)$ for the two devices. Note that device B2 underwent one thermal cycling to room temperature and cooled down again for a second-rum measurement, then relabeled B2m. The amplitude of ZBCP of B2m is notably reduced from that of B2, while T_c^{onset} is reduced from 2.33 K in B2 to 2.03 K in B2m.

Thermal cycling effect

Besides varying the thermal annealing temperature T_a we also studied the effect of thermal cycling on the device properties. Thermal cycle consisted of heating the device up to $\sim$ 300 K (room temperature) and cooling it down again to the sub-kelvin range.

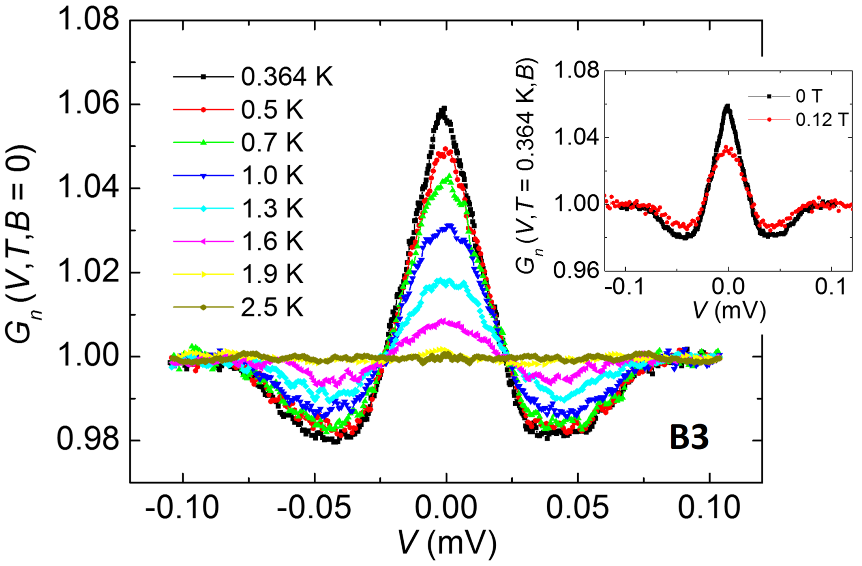

FIG. S5. Finite-bias $G_n(V, T, 0)$ of device B3 measured at several T values. The amplitude of the ZBCP gradually decreases as T increases. The inset demonstrates the magnetic field dependence. Shown is the ZBCP at $T = 0.364\,\mathrm{K}$ and $B = 0.12\,\mathrm{T}$.

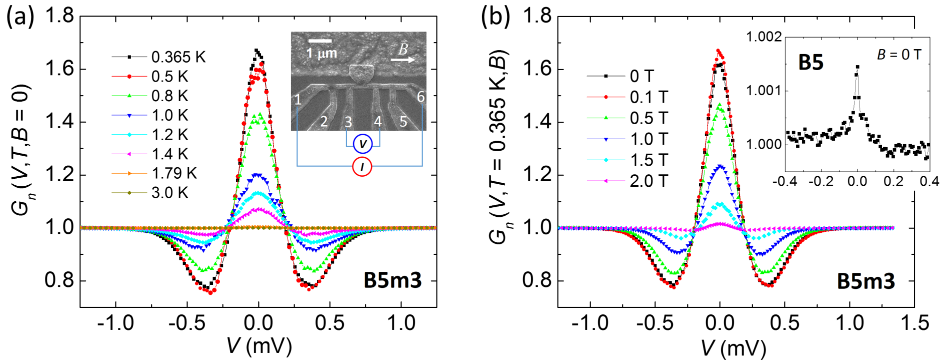

FIG. S6. Normalized conductance spectra of device B5m3 measured with voltage-electrode (VE) pair (3,4). (a) Finite-bias $G_n(V, T, 0)$ at several T values. The amplitude of ZBCP gradually decreases with increasing T, persisting up to about 1.79 K. The inset shows an SEM image of the device with the 4-probe configuration indicated. (b) Finite-bias $G_n(V, 0.365\,\mathrm{K}, B)$ in several B fields. The amplitude of the ZBCP diminishes as B increases. Inset: $G_n(V, 0.37\,\mathrm{K}, 0)$ of the as-grown device B5, also measured with the VE pair (3,4). It is significantly smaller than that of device B5m3.

After the conductance spectra of the as grown device B1 (B2) were measured at low temperatures, the device was warmed up from 0.36 K to 300 K and cooled down again for a second-run measurement of the conductance spectra. The device was then labeled B1m (B2m), because the device properties (e.g., the transparency of the S/N interface as well as the defect configurations of the $TiSi_2$ component) were often sensitive to thermal cycling and repeated finite-bias measurements. Device B5 was intentionally subject to three times of thermal cycling to check the robustness and reproducibility of the conductance spectra. Thus, B5m3 denotes the fourth-run measurement of device B5.

As for the effect of the thermal cycling, one expects that thermal cycling up to 300 K of a device formed at high annealing temperature will transform such a C54 rich device into a predominantly C49 device. This is borne out by device B5 turning into B5m3. On the other hand, the C49 phase is rich in lattice faults and mismatches that contribute to its diffusive properties. Thermal cycling of a device that consists essentially of the C49 phase may affect the distribution of defects and faults but the overall changes should be comparatively small when compared to that of the C54 → C49 case. This is indeed observed in device B1 turning into B1m as well as B2 into B2m. Therefore, a naive understanding of the C49/C54 properties is sufficient for a qualitative understanding of the effect of annealing and thermal cycling. A complete stability analysis of the structural properties of $TiSi_2$ in confined geometries remains, however, challenging [5] as the stability of the C49 phase is affected by the annealing temperature, the substrate surface, layer thickness, and the possible occurrence of electromigration [7].

Ginzburg-Landau analysis of the enhanced interface two-component superconductivity

The Ginzburg-Landau (GL) free energy for a system with broken inversion symmetry in one-dimensional representation reads [8],

$$\mathbf{F} = \int d\vec{r}\,[\mathcal{F}_0 + \mathcal{F}_c + \mathcal{F}_n + \mathcal{F}_B + \mathcal{F}_{me} + \mathcal{F}_{pol}] \tag{S1}$$

here $\mathcal{F}_0 = \sum_\nu \left(a_\nu(x)|\Phi_\nu|^2 + b_\nu|\Phi_\nu|^4 + K_\nu|\vec{D}\Phi_\nu|^2\right)$ is the usual GL free energy for each individual component, the subscript $\nu = \pm$ represents the two components of the order parameter, and $\vec{D} = \vec{\nabla} - 2\pi i/\Phi_0\vec{A}$, where $\vec{A}$ is the vector potential, and Φ_0 is the magnetic flux quantum. The coefficient a_ν is $\alpha_\nu(T - T_{c\nu})$, while $K_\pm$ in general depends on the electronic mean free path. We take the superconductor to be in the clean limit and assume $K_\pm = K_s$. $\mathcal{F}_c = c(x)\left(\Phi_+^*\Phi_- + \Phi_+\Phi_-^*\right)$ is the coupling between the two components, a negative value of the coefficient c ensures that both order parameters have the same phase and $\mathcal{F}_n$ is the free energy density of the non-superconducting state in the absence of a magnetic field (H). $\mathcal{F}_B = \vec{B}^2/(8\pi)$ is the contribution from the magnetic field. $\mathcal{F}_{me} = \sum_\nu iK_{me,\nu}(\vec{H}\times\hat{z})\cdot\left[\Phi_\nu^*(\vec{D}\Phi_\nu) - h.c.\right]$ is a Lifshitz invariant term leads to magneto-electric coupling and $\mathcal{F}_{pol} = \sum_{\nu,i} Q_{\nu i}|\Phi_\nu|^2H_i^2$ determines the effect of superconducting order on spin-polarization, where subscript $i = x, y, z$ denotes the spatial dimensions. To find the ground state, we minimize the GL free energy, which results in,

$$\begin{aligned} K_s\partial_{x^2}\Phi_+ &= \left(a_+ + K_s\gamma^2H^2x^2 + QH^2\right)\Phi_+ \\ &+ 2b_+|\Phi_+|^2\Phi_+ + c\Phi_- + 2iK_{me+}H\partial_x\Phi_+, \end{aligned} \tag{S2}$$

$$\begin{aligned} K_s\partial_{x^2}\Phi_- &= \left(a_- + K_s\gamma^2H^2x^2 + QH^2\right)\Phi_- \\ &+ 2b_-|\Phi_-|^2\Phi_+ + c\Phi_+ + 2iK_{me-}H\partial_x\Phi_-. \end{aligned} \tag{S3}$$

Here $\gamma = 2\pi/\Phi_0$, where Φ_0 is the magnetic flux quanta, and we set the vector potential $\vec{A} = (0, 0, -Hx)$, which gives the magnetic field in the $\hat{y}$ direction. All lengths can be expressed in terms of the coherence length $\xi_0^{-2} = N_0T_c/2K_s$, where the coefficient K_s is $7\zeta(3)N_0v_F^2/64\pi^2T_c^2$, v_F is the average Fermi velocity, and N_0 is the density of states. Here T_c refers to the bulk transition temperature. We assume an isotropic Fermi-surface and ignore the difference in the Fermi velocities and density of states of two helical bands formed due to the spin-orbit coupling. Similarly, the magnetic field can be measured in unit of $\tilde{H}_{c2}^{\mathrm{bulk}}$, which is $\Phi_0/(2\pi\xi_0^2)$ and all energies in these equations can be expressed in units of T_c. The coefficient a_ν is $N_0(T - T_{c\nu})/2$. The coefficient Q is,

$$Q = \frac{7\zeta(3)\mu_B^2N_0}{16\pi^2T_c^2}, \tag{S4}$$

where μ_B is the Bohr magneton. The magneto-electric coefficient $K_{me\pm}$ has opposite sign for two helical bands [8], and it reads,

$$K_{me\pm} = \mp\mu_B\frac{7\zeta(3)}{4\pi^2T_c^2}\frac{N_0v_F}{4}. \tag{S5}$$

We further assume $b_\pm = b$. Equations (S2) and (S3) augmented with De Gennes's boundary condition for the superconductor - normal metal interface are solved. The De Gennes's boundary condition is a general boundary condition for superconductors interfacing with insulators or normal metals, depending on the value of the extrapolation length (which approaches infinity for an insulator). This boundary condition arises from an order parameter expansion of the interface contribution to the free energy[9]. In our approach, we get the enhanced superconductivity through the spatial dependence of the quadratic terms in the GL free energy[10]. The interface driven enhancement can be also modelled with a negative extrapolation length[11], however, we avoid using a negative value for a physical length scale, because the modification of the quadratic terms near the interface is more likely to happen from a microscopic viewpoint. The results are shown in Fig. S7 for various values of the magnetic field, and it shows that the order parameters remain finite up to several coherence lengths from the S/N interface.

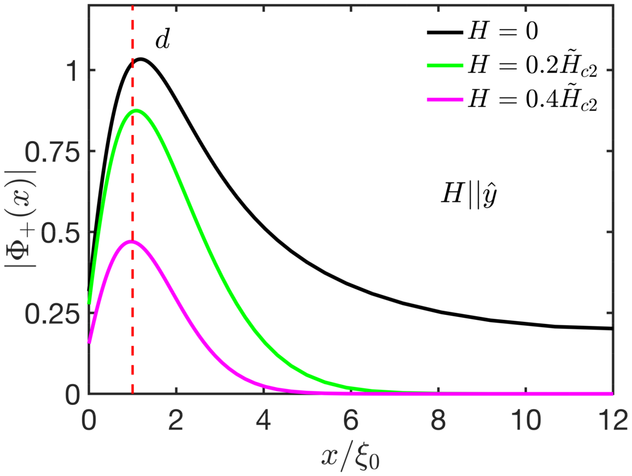

FIG. S7. Absolute value of the dominant component Φ_+ is plotted as a function of distance x for several values of the magnetic field at $T = 1.2T_c$ for $d = \xi_0$ and $\ell = 0.25\xi_0$. The S/N interface is located at $x = 0$. The effective thickness of the interface layer (d) is indicated.

[1] Y. Asano, Y. Tanaka, A. A. Golubov, and S. Kashiwaya, Phys. Rev. Lett. **99**, 067005 (2007).
[2] Z. Ma and L. H. Allen, Phys. Rev. B **49**, 13501 (1994).
[3] H. Jeon, C. A. Sukow, J. W. Honeycutt, G. A. Rozgonyi, and R. J. Nemanich, J. Appl. Phys. **71**, 4269 (1992).
[4] S.-P. Chiu, C. C. Tsuei, S.-S. Yeh, F.-C. Zhang, S. Kirchner, and J.-J. Lin, Science Advances **7**, eabg6569 (2021).
[5] C. Colinet, W. Wolf, R. Podloucky, and A. Pasturel, Appl. Phys. Lett. **87**, 041910 (2005).
[6] F. Mammoliti, M. G. Grimaldi, and F. La Via, J. Appl. Phys. **92**, 3147 (2002).
[7] K. N. Tu, J. Appl. Phys. **94**, 5451 (2003).
[8] M. Sigrist, AIP Conference Proceedings **1162**, 55 (2009).
[9] M. Sigrist and H. Monien, Journal of the Physical Society of Japan **70**, 2409 (2001).
[10] H. Kaneyasu, Y. Enokida, T. Nomura, Y. Hasegawa, T. Sakai, and M. Sigrist, Phys. Rev. B **100**, 214501 (2019).
[11] A. Samoilenka and E. Babaev, Phys. Rev. B **101**, 134512 (2020).